10.2514/6.2014-1030

AIAA SciTech Forum
13-17 January 2014, National Harbor, Maryland
52nd Aerospace Sciences Meeting

Experimental and numerical study of fast gas heating and O atom production in a capillary nanosecond discharge

Andrei V. Klochko[1], Arthur Salmon[2] and Joseph Lemainque[2]
Laboratory of Plasma Physics (CNRS, Ecole Polytechnique, Sorbonne Universities, UPMC Univ. Paris 06, University Paris-Sud) Palaiseau, 91128, France

Nikolay A. Popov[3]
Skobeltsyn Institute for Nuclear Physics, Moscow State University, Moscow, 119991, Russia

Jean-Paul Booth[4]
Laboratory of Plasma Physics (CNRS, Ecole Polytechnique, Sorbonne Universities, UPMC Univ. Paris 06, University Paris-Sud) Palaiseau, 91128, France

Zhongmin Xiong[5] and Mark J. Kushner[6]
University of Michigan, Dept. of Electrical Engineering and Computer Science, Ann Arbor, MI 48109-2122, USA

and

Svetlana M. Starikovskaia[4]
Laboratory of Plasma Physics (CNRS, Ecole Polytechnique, Sorbonne Universities, UPMC Univ. Paris 06, University Paris-Sud) Palaiseau, 91128, France

A nanosecond repetitively pulsed discharge in a quartz capillary filled with flowing synthetic air was investigated as a benchmark to address the mechanism of fast gas heating for conditions of up to complete dissociation of O_2 and heating of a few thousand K occurring during the near afterglow phase. Electric current, electric field, gas temperature, energy deposition, and O atom concentrations were measured with respect to time. A 2-dimensional model was used to simulate discharge initiation and early breakdown, while a detailed 0D kinetic model was used to address the afterglow phase and fast gas heating. The high oxygen dissociation degree enables investigation of the key role played by O atoms in the fast gas heating chemistry.

I. Introduction

NANOSECOND repetitively pulsed discharge plasmas are attractive for applications from plasma assisted combustion[1] to aerodynamic flow control at high Mach number[2]. These attractive features include the low average power required to run such discharges (because of their pulsed nature) and their high energy efficiency to produce radicals and electronically excited species[3] which in turn contribute to fast gas heating[4]. Fast gas heating

[1] PhD Student, Laboratory for Plasma Physics, Ecole Polytechnique, Route de Saclay, 91128 Palaiseau Cedex, France, AIAA Student member.
[2] Master Student, Laboratory for Plasma Physics, Ecole Polytechnique, Route de Saclay, 91128 Palaiseau Cedex, France.
[3] Senior Researcher, Skobletsyn Institute for Nuclear Physics, Moscow State University, Leninskie gory, GSP-1, Moscow 119991, Russian Federation, AIAA Member.
[4] Senior Researcher, Laboratory for Plasma Physics, Ecole Polytechnique, Route de Saclay, 91128 Palaiseau Cedex, France.
[5] Assistant Research Scientist, University of Michigan, 2236 EECS Bldg., 1301 Beal Ave, Ann Arbor, Michigan 48109-2122 USA.
[6] Senior Researcher, Director, University of Michigan, 2236 EECS Bldg., 1301 Beal Ave, Ann Arbor, Michigan 48109-2122 USA.

refers to a significant increase in gas temperature over a time shorter than the gas dynamic time, that would normally be required to obtain the same heating by purely mechanical means.

Fast gas heating can enhance the rate of endothermic chemical reactions, leading to faster ignition of combustible mixtures even at low initial gas temperatures[3]. Fast gas heating is therefore useful in combustion enhancement techniques. Such gas heating may produce shock waves, perturb flow and prevent instabilities, even in high enthalpy flows, which motivates its use in aerodynamic flow control[5].

Fast gas heating, however, involves kinetic mechanisms that may be complex and which may vary depending on the conditions[4]. These conditions include the gas composition (including radicals and excited species from prior pulses), and the reduced electric field (E/N) which will determine the main channels through which the energy of the discharge will be deposited.

In this paper, we will discuss the properties of capillary electrical discharges in which fast gas heating occurs based on experimental results and modeling. We found that processes during initiation of the discharge and the early breakdown phase are well explained by results from collaborative measurements and modeling. The experimental results for O atom concentrations in the post-discharge and predictions from detailed kinetic modeling also generally agree.

The experiment, including TALIF and actinometry diagnostics, will be described in Sec. II. Descriptions of the two numerical models that were used to simulate different aspects of the experiment are in Sec. III. These models are a 2D axisymmetric model used to simulate the fast ionization wave development and early breakdown and a 0D kinetic model used to predict O atom density in the post-discharge phase. Experimental and computational results are discussed in Sec. IV and our conclusions are in Sec. V.

II. Description of the Experiment

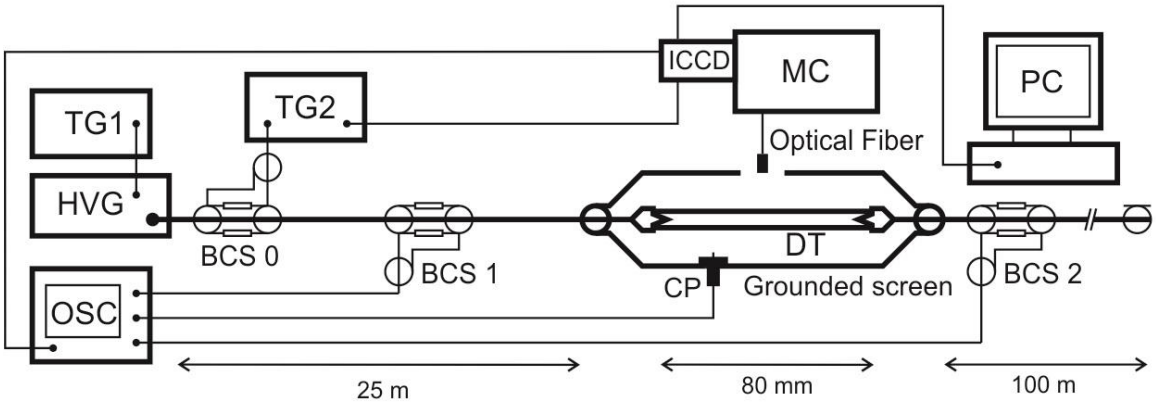

Figure 1. Experimental setup. *DT - Discharge tube; BCS - Back Current Shunt; TG - Triggering generator; HVG - High Voltage Generator; CP - Capacitive Probe; ICCD - Intensified CCD Camera; OSC - Oscilloscope; MC - Monochromator*

A schematic of the experimental setup for electrical and spectroscopic measurements is shown in Fig. 1. The discharge is initiated in a quartz capillary tube, 1.5 mm in diameter and 80 mm in length. The capillary is filled with flowing synthetic air at a pressure 13-30 mbar with a 50 sccm rate, insuring efficient gas renewal between pulses. The discharge takes the form of a fast ionization wave (FIW), followed by an energy deposition phase, during which a spatially uniform reduced electric field (E/N ≈150-300 Td, 1 Td = 10^{-17} V-cm^2) coexists with a high electric current of about 70-100 A. The voltage pulse (29 ns FWHM, 9.8 kV amplitude, and 4 ns rise time) is supplied by a FID FPG 10-MKS20 high voltage generator through a 25 m coaxial RG213 cable. Three pulses separated by 250 ns are incident on the capillary tube due to successive reflections between the generator and the discharge assembly.

The discharge tube is terminated by two metal pin-shaped electrodes connected to two cables. The cable from the generator is connected to the HV electrode. The other cable, connected to the LV electrode, is left unterminated. A delayed pulse one microsecond after initial breakdown is produced as this cable acts as a delay line. Both cables are 50 Ohm, which allows current and voltage profiles to be measured by Back Current Shunts (BCS). These shunts are located 12.5 m before and after the discharge assembly on the HV and delay cables. The discharge is surrounded by a grounded aluminum screen. The discharge geometry is coaxial, so that the voltage pulse can be transmitted from the HV cable to the delay cable, through the discharge capillary tube.

A capacitive detector, inserted in a slit of the upper screen, provides local voltage measurements above different regions of the tube which are then converted to electric field. For spectroscopy, the capacitive detector is replaced by a fiber optic mount to collect light. The spectral system consists of an Andor SR-303i monochromator, with an Andor DH734-18U-03 ICCD camera. The spectrometer is used both for temperature measurements - based on the rotational distribution of the $N_2(C^3\Pi_u, v = 0) \rightarrow N_2(B^3\Pi_g, v = 1)$ transition - and for actinometric measurements of O atom concentrations in the discharge.

A. Electrical diagnostics

Two types of electrical diagnostics are used in this discharge setup: two back current shunts, and a capacitive probe.

The back current shunts (BCS) consist of arrays of identical low-inductance resistors, that replace the grounded outer conductor of a coaxial cable, in a 3 cm long section. The voltage drop is then measured across that array to obtain voltage and current profiles in the long high voltage cable in which the shunt is inserted. A detailed description of back current shunts can be found in Ref. 6.

The capacitive detector is a divider that provides a direct measurement of the electric potential at its location and, by calibration, in the discharge tube. The probe consists of a metal tip, at floating potential, that protrudes from the grounded screen that shields the discharge. This tip is connected through a 400 pF coaxial capacitor to the oscilloscope. The detector can be slid along the slit providing measurements each mm above the discharge. A schematic and image of the capacitive detector are in Fig. 2.

The electric potential measured at the detector is related to the potential at the discharge tube inner surface by

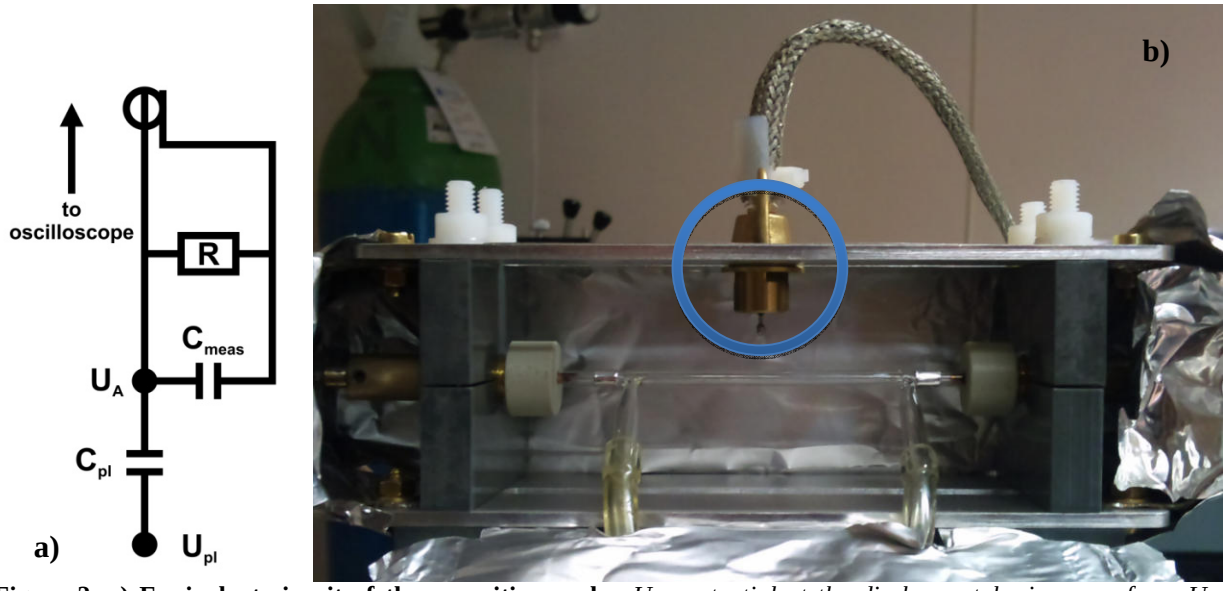

Figure 2. a) Equivalent circuit of the capacitive probe. *U_{pl}: potential at the discharge tube inner surface; U_A: potential of the capacitive detector tip; C_{pl}: capacitance of the detector tip/discharge tube ensemble; C_{meas}: coaxial capacitor through which the signal is collected; R: impedance of the cable (50 Ohm), connecting the detector to a 50 Ohm port of the oscilloscope.* **b) Discharge assembly, showing the capacitive probe.** *The capacitive probe is circled in blue. The aluminum tape that can be seen behind the discharge is part of the grounded screen.*

$$U_A = \frac{U_{pl} j\omega C_{pl}}{\frac{1}{R} + j\omega C_{meas} + j\omega C_{pl}} \tag{1}$$

$$U_{pl} = U_A\left(1 + \frac{C_{meas}}{C_{pl}}\right) + \frac{1}{j\omega R C_{pl}} U_A \tag{2}$$

$$U_{pl}(t) = \alpha\left(U_A(t) + \frac{1}{\tau}\int_{t'=0}^{t} U_A(t')dt'\right) \tag{3}$$

with $\alpha = 1 + C_{meas}/C_{pl}$ and $\tau = R(C_{meas} + C_{pl})$. The probe is calibrated as follows. The air plasma is replaced by a 1 mm diameter copper wire connected to both the HV and LV electrodes. The rest of the system remains unchanged. A high voltage pulse is transmitted without significant loss from the HV to the LV electrode so that the potential at the surface of the wire is close to that provided by the generator. The two parameters α and τ are then adjusted so that the signal produced by the capacitive probe closely corresponds to the values provided by the shunt probes. The end result is shown in Fig. 3. Detector signals at different axial locations are assembled to provide voltage profiles, and then differentiated to produce electric field.

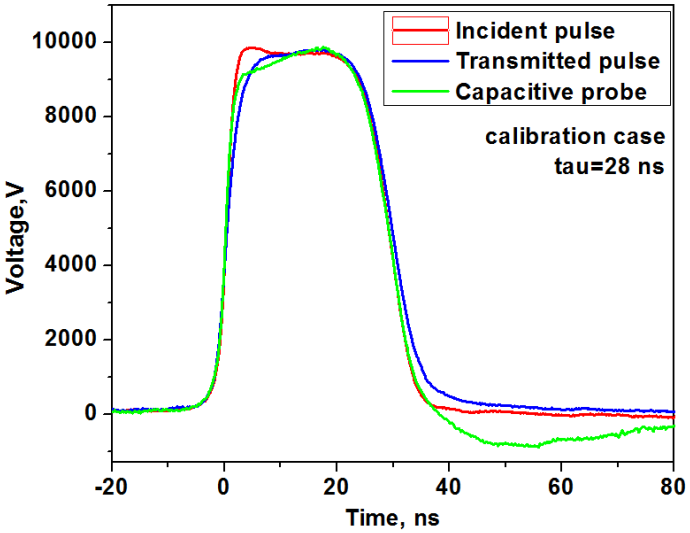

Figure 3. calibration of the capacitive probe, compared to incident and transmitted pulses. *The calibration case corresponds to a metal wire connecting the two electrodes replacing the air plasma.*

B. Actinometric measurements

In order to measure O atom concentrations in our discharge, two techniques were used: actinometry, and two-photon absorption laser induced fluorescence (TALIF). For the actinometry[7-9], Argon was added to the synthetic air to a mole fraction of 4%. Radiation from the $\mathrm{Ar}(2p_1) \rightarrow \mathrm{Ar}(1s_2)$ transition, at 750.4 nm and the $\mathrm{O}(3p^3P) \rightarrow \mathrm{O}(3s^3S)$ transition at 844.6 nm were compared. The signal was integrated in wavelength across the line width. A 590 nm long-pass filter was used to screen the second order of the powerful UV emission of the discharge. In order to convert this intensity ratio to absolute O atoms densities the following procedure was used.

First, the rate equations for the excited Oxygen and Argon atoms are:

$$\frac{d[\mathrm{O}^*]}{dt} = k_e^{\mathrm{O}} n_e[\mathrm{O}] + k_{de}^{\mathrm{O}} n_e[\mathrm{O}_2] + k_e^{\mathrm{O}(^1\mathrm{S})} n_e[\mathrm{O}(^1\mathrm{S})] + k_e^{\mathrm{O}(^1\mathrm{D})} n_e[\mathrm{O}(^1\mathrm{D})] - \frac{[\mathrm{O}^*]}{\tau_{\mathrm{O}^*}} - [\mathrm{O}^*] \sum_i k_{Q,i}^{\mathrm{O}^*} [\mathrm{Q}_i] \quad (4)$$

$$\frac{d[\mathrm{Ar}^*]}{dt} = k_e^{\mathrm{Ar}} n_e[\mathrm{Ar}] - \frac{[\mathrm{Ar}^*]}{\tau_{\mathrm{Ar}^*}} - [\mathrm{Ar}^*] \sum_i k_{Q,i}^{\mathrm{Ar}^*} [\mathrm{Q}_i] \quad (5)$$

Here k_e^{X} is the excitation rate constant from X state to $\mathrm{O}(3p^3P)$ in (4), and $\mathrm{Ar}(2p_1)$ in (5); k_{de}^{O} is the dissociative excitation rate constant for molecular oxygen; $k_{Q,i}^{\mathrm{X}^*}$ is the quenching rate constant for species X^* by species Q_i; n_e is the electron density; and τ_{X^*} is the radiation decay lifetime of species X^*. These equations can be rewritten as :

$$\frac{d[\mathrm{O}^*]}{dt} + \frac{[\mathrm{O}^*]}{\tau_{\mathrm{O}^*}} + [\mathrm{O}^*] \sum_i k_{Q,i}^{\mathrm{O}^*} [\mathrm{Q}_i] = k_e^{\mathrm{O}} n_e[\mathrm{O}] + k_{de}^{\mathrm{O}} n_e[\mathrm{O}_2] + k_e^{\mathrm{O}(^1\mathrm{S})} n_e[\mathrm{O}(^1\mathrm{S})] + k_e^{\mathrm{O}(^1\mathrm{D})} n_e[\mathrm{O}(^1\mathrm{D})] \quad (4')$$

$$\frac{d[\mathrm{Ar}^*]}{dt} + \frac{[\mathrm{Ar}^*]}{\tau_{\mathrm{Ar}^*}} + [\mathrm{Ar}^*] \sum_i k_{Q,i}^{\mathrm{Ar}^*} [\mathrm{Q}_i] = k_e^{\mathrm{Ar}} n_e[\mathrm{Ar}] \quad (5')$$

$$\frac{\frac{d[\mathrm{O}^*]}{dt} + \frac{[\mathrm{O}^*]}{\tau_{\mathrm{O}^*}} + [\mathrm{O}^*] \sum_i k_{Q,i}^{\mathrm{O}^*} [\mathrm{Q}_i]}{\frac{d[\mathrm{Ar}^*]}{dt} + \frac{[\mathrm{Ar}^*]}{\tau_{\mathrm{Ar}^*}} + [\mathrm{Ar}^*] \sum_i k_{Q,i}^{\mathrm{Ar}^*} [\mathrm{Q}_i]} = \frac{k_e^{\mathrm{O}}[\mathrm{O}] + k_{de}^{\mathrm{O}}[\mathrm{O}_2] + k_e^{\mathrm{O}(^1\mathrm{S})}[\mathrm{O}(^1\mathrm{S})] + k_e^{\mathrm{O}(^1\mathrm{D})}[\mathrm{O}(^1\mathrm{D})]}{k_e^{\mathrm{Ar}}[\mathrm{Ar}]} \quad (6)$$

The emission intensities are related to atomic densities by:

$$I_{844} = c_{844}\,[\mathrm{O}^*]/\tau_{\mathrm{O}^*} \tag{7}$$

$$I_{750} = c_{750}\,[\mathrm{O}^*]/\tau_{\mathrm{O}^*} \tag{8}$$

Where c_{XXX} is the optical collection efficiency factor for wavelength XXX. The intensity here corresponds to a photon count. When inserting equations (7) and (8) into (6), we get:

$$\frac{\tau_{O^*}}{\tau_{Ar^*}}\frac{c_{750}}{c_{844}}\frac{\frac{dI_{844}}{dt}+\frac{I_{844}}{\tau_{\mathrm{O}^*}}+I_{844}\sum_i k_{Q,i}^{\mathrm{O}^*}[\mathrm{Q}_i]}{\frac{dI_{750}}{dt}+\frac{I_{750}}{\tau_{\mathrm{Ar}^*}}+I_{750}\sum_i k_{Q,i}^{\mathrm{Ar}^*}[\mathrm{Q}_i]} = \frac{k_e^{\mathrm{O}}[\mathrm{O}]+k_{de}^{\mathrm{O}}[\mathrm{O}_2]+k_e^{\mathrm{O}(^1\mathrm{S})}[\mathrm{O}(^1\mathrm{S})]+k_e^{\mathrm{O}(^1\mathrm{D})}[\mathrm{O}(^1\mathrm{D})]}{k_e^{\mathrm{Ar}}[\mathrm{Ar}]} \tag{9}$$

$$\frac{k_e^{\mathrm{O}}[\mathrm{O}]}{k_e^{\mathrm{Ar}}[\mathrm{Ar}]} = \frac{\tau_{O^*}}{\tau_{Ar^*}}\frac{c_{750}}{c_{844}}\frac{\frac{dI_{844}}{dt}+\frac{I_{844}}{\tau_{\mathrm{O}^*}}+I_{844}\sum_i k_{Q,i}^{\mathrm{O}^*}[\mathrm{Q}_i]}{\frac{dI_{750}}{dt}+\frac{I_{750}}{\tau_{\mathrm{Ar}^*}}+I_{750}\sum_i k_{Q,i}^{\mathrm{Ar}^*}[\mathrm{Q}_i]} - \frac{k_{de}^{\mathrm{O}}[\mathrm{O}_2]+k_e^{\mathrm{O}(^1\mathrm{S})}[\mathrm{O}(^1\mathrm{S})]+k_e^{\mathrm{O}(^1\mathrm{D})}[\mathrm{O}(^1\mathrm{D})]}{k_e^{\mathrm{Ar}}[\mathrm{Ar}]} \tag{10}$$

$$[\mathrm{O}] = \frac{k_e^{\mathrm{Ar}}[\mathrm{Ar}]}{k_e^{\mathrm{O}}}\frac{\tau_{O^*}}{\tau_{Ar^*}}\frac{c_{750}}{c_{844}}\frac{\frac{dI_{844}}{dt}+\frac{I_{844}}{\tau_{\mathrm{O}^*}}+I_{844}\sum_i k_{Q,i}^{\mathrm{O}^*}[\mathrm{Q}_i]}{\frac{dI_{750}}{dt}+\frac{I_{750}}{\tau_{\mathrm{Ar}^*}}+I_{750}\sum_i k_{Q,i}^{\mathrm{Ar}^*}[\mathrm{Q}_i]} - \frac{k_{de}^{\mathrm{O}}[\mathrm{O}_2]+k_e^{\mathrm{O}(^1\mathrm{S})}[\mathrm{O}(^1\mathrm{S})]+k_e^{\mathrm{O}(^1\mathrm{D})}[\mathrm{O}(^1\mathrm{D})]}{k_e^{\mathrm{O}}} \tag{11}$$

This expression does not take into account the depletion of the O_2 quencher for Argon, which is important because the $\mathrm{Ar}(2\mathrm{p}_1)$ state is not strongly quenched by molecular nitrogen. We also did not include excitation transfer between metastable $\mathrm{Ar}(^3\mathrm{P}_{2,0})$ atoms and excited $\mathrm{O}(3\mathrm{p}^3\mathrm{P})$ atoms[10], quenching of $\mathrm{O}(3\mathrm{p}^3\mathrm{P})$ and $\mathrm{Ar}(2\mathrm{p}_1)$ by atomic oxygen, and dependence of quenching rates on gas temperature.

The concentrations of excited species are calculated using ZDPlasKin[11]. The reaction mechanism is based on Kossyi[12]. The detailed reaction mechanism and tuning of ZDPlasKin are described in Ref. 13.

C. TALIF measurements

In order to measure O atom densities later in the afterglow when optical emission is weak, TALIF measurements were made. When excited by 225.58 nm radiation (all wavelengths are given in air), an oxygen atom can absorb two photons and access the $\mathrm{O}(3\mathrm{p}^3\mathrm{P})$ excited state, from which it radiates to the $\mathrm{O}(3\mathrm{s}^3\mathrm{S})$ state by emitting one photon at 844.6 nm. The intensity of this fluorescence is directly proportional to the local density of O atoms. To obtain an absolute value of the O atom concentration, a calibration is made by replacing the air plasma by xenon gas alone. When excited by 224.24 nm radiation, Xe emits light in the infrared (834.68nm). By comparing the TALIF signal from O atoms and from the known density of Xe, one can deduce the absolute concentration of O atoms. This procedure is discussed in Ref. 14. The procedure that was used to convert relative TALIF data points into absolute O atom densities in our configuration, was the same as described in detail in our previous paper[15].

1. Laser system and light collection optics

A schematic of the TALIF experimental setup is in Fig. 4. A tripled Nd:YAG laser (355 nm) was used to pump a Coumarin 2 dye laser (peak efficiency at 450 nm) which was then doubled to obtain wavelengths around 225.58 nm (for O atoms) and 224.24 nm (for Xe atoms). The resulting beam was approximately 5 mm in diameter, its temporal FWHM was around 10 ns, and it was repeated at a frequency of 10 Hz. The beam energy was measured by an amplified energy meter, with sensitivity 1100 V/J, installed after the discharge tube. The laser energy inside the capillary was varied between 200 and 1 μJ by means of a variable attenuator.

An optical fiber placed above the discharge was used to collect the fluorescence light through a narrow bandpass filter, and was detected by a Hamamatsu R3896 red-sensitive photomultiplier tube (PMT) connected to a Lecroy WR64-Xi oscilloscope. The transmission of the optical fiber and bandpass filter were measured separately using an Energetiq EQ-99 LDLS calibration lamp.

The laser controller is the synchronization master. The discharge takes place at a given delay before the laser light arrives. This delay is varied from 2200 ns before to 800 ns after the laser pulse, with a variability of ±20 ns, with rare events at ±200 ns due to the jitter in the HV nanosecond generator. Each time the laser is fired, the PMT

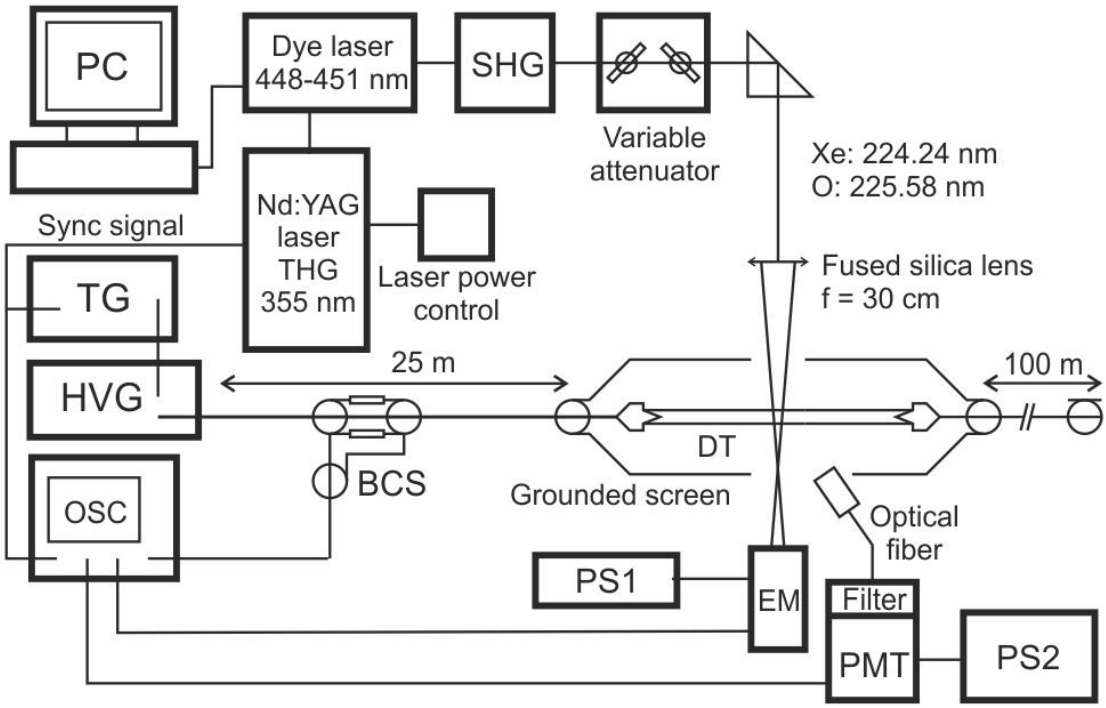

Figure 4. Experimental setup for the TALIF measurement. *SHG/THG: Second/Third Harmonic Generation; TG: Triggering generator; HVG: High Voltage Generator; OSC: Oscilloscope; BCS: Back Current Shunt; DT: Discharge tube; EM: Energy meter; PS: Power supply; PMT: Photomultiplier; PC: Computer.*

registers a fluorescence time profile. In order to obtain absolute O atom concentrations at a given pressure and delay, the laser is then scanned in wavelength across the $O(3p^3P)$ absorption line, thereby producing a series of fluorescence profiles. Each of these profiles is then integrated in time, and the resulting values are then integrated in wavelength to produce a relative TALIF data point. This data point is then calibrated by the measurements in Xe.

Due to the small size, high curvature, and low UV quality of the quartz capillary in which the discharge takes place, special care needs to be taken in order to perform a TALIF measurement directly in the capillary. The experiment was made strongly out of focus (6 cm away from the focal point of a Suprasil lens with a 30 cm focal length) to prevent optical damage. Care was taken not to be in a configuration where light would focus somewhere inside the capillary walls. A simple 2D ray tracing program was used to estimate the trajectory of light rays in the capillary. Finally, as the laser beam becomes strongly divergent after crossing the capillary, part of the energy of the beam, especially the energy that was outside the 5 mm wide core, does not reach the energy meter. To compensate for this effect, the energy was also measured before the lens. The evolution of the ratio of the energy before and after the capillary was monitored to compensate any drift in the experiment.

III. Numerical modeling

A. Description of the 2D model: FIW propagation and discharge development

Two-dimensional (2D) simulations of the ns discharge dynamics in the capillary tube were performed using *nonPDPSIM*, a plasma hydrodynamics model with radiation transport[16-17]. Based on 2-d unstructured finite volume discretization, *nonPDPSIM* solves the transport equations for all charged species and Poisson's equation for electric potential using a fully implicit Newton's method. Updates of the charged particle densities and electric potential are followed by an implicit update of the electron temperature, T_e, neutral particle densities, beam electron transport and neutral flow field properties using a modified version of the Navier-Stokes equations. In the present study, the plasma species included in model are the ground states of N_2 and O_2, the N_2 vibrational states(v=1-8), 5 excited states (N_2^*, O_2^*, N_2^{**}, N^*, O^*), 3 atomic states (N, O, O_3) and 9 charged species (e, N_2^+, O_2^+, N^+, O^+, N_4^+, O_4^+, O_2^-, O^-). The total number of electro-chemical reactions is about 180. To facilitate the propagation of the positive ionization wave, the photoionization of O_2 by the UV flux from the radiating N_2^{**}(Birge-Hopfield band, $b'^1\Sigma_u^+, b^1\Pi_u \rightarrow X^1\Sigma_g^+$) was included with a cross-section varying between 1 to 5 × 10^{-16} cm^2. Secondary electron emission from plasma bounding surfaces due to ion bombardment was also included with a secondary emission coefficient $\gamma = 0.1$. The secondary electron emission produced by photon bombardment was neglected for simplicity.

The discharge configuration used in the 2-d model is based on the experimental setup but assumed to be axisymmetric. The geometry includes the high (HV) and low voltage (LV) electrodes, the grounded metal screen shield having a radius of 2.4 cm and the discharge capillary tube itself (quartz, ε_r= 4). The inner and outer diameters of the capillary are 0.15 cm and 0.34 cm, and the distance between HV and LV electrode tips is 8 cm. The capillary is filled with synthetic air (N_2:O_2=4:1) at 27 mbar and 300 K and forced gas flow is neglected. Note that because of the axisymmetric nature, the metal shield in the model is cylindrical instead of the two flat screens placed above and below the capillary in the experiments. A 20 kV voltage pulse of 35 ns length (about 6 ns rise time and 8 ns fall time) was applied to the HV electrode to initiate and sustain the discharges. The initial electron density was assumed to be [e] = 10^9 cm^{-3} uniformly distributed in the capillary to account for the residual electron density from prior pulses that occurs in the experiment. The total number of grid points was about 20,000, of which about 15,000 are distributed in the plasma zone with the mesh size varying between 50 µm and 100 µm.

B. Description of the 0D detailed kinetic model: discharge, afterglow and O atom production

A 0D global kinetic model was used to predict the density of O atoms generated by the discharge over the first two microseconds and the electric field within the plasma column. These predictions were then compared to experimental measurements based on TALIF and actinometry techniques. The model takes as input parameters:

- The electric current density, calculated from the total electric current in the middle of the tube (at equal distance from the two electrodes) and the tube inner cross section (1.5 mm diameter) during the three main discharge pulses at 0, 250 and 500 ns.

- The gas initial composition, N_2/O_2 = 80/20; temperature, 300 K; and initial gas density (based on the pressures of 24, 27 or 30 mbar).

The model and reaction mechanism are described in detail in Ref. 4. The correlation of the calculated gas temperature with experimental measurements was demonstrated in Ref. 15. The primary reactions leading to the production and losses of O atoms are in Table 1.

	Reaction	Coefficient (cm^3/s)	Ref
(R1)	$e + O_2 \rightarrow O(^3P) + O(^3P)$	$\sigma_1(E/N)$	[18, 19]
(R2)	$e + O_2 \rightarrow O(^3P) + O(^1D)$	$\sigma_2(E/N)$	[18, 19]
(R3)	$N_2(A^3\Sigma_u^+) + O_2 \rightarrow N_2(v) + 2O(^3P)$	$1.7x10^{-12}$	[12]
(R4)	$N_2(B^3\Pi_g) + O_2 \rightarrow N_2(v) + 2O(^3P)$	$3.0x10^{-10}$	[4, 12]
(R5)	$N_2(a'^1\Sigma_u^-) + O_2 \rightarrow N_2(v) + O(^3P) + O(^1D)$	$2.8x10^{-11}$	[4, 12]
(R6)	$N_2(C^3\Pi_u) + O_2 \rightarrow N_2 + O(^3P) + O(^1D)$	$2.5x10^{-10}$	[4, 12]
(R7)	$N_2(A^3\Sigma_u^+) + O(^3P) \rightarrow NO + N(^4S, ^2D)$	$3.0x10^{-11}$	[12, 15]
(R8)	$N_2(B^3\Pi_g) + O(^3P) \rightarrow NO + N(^4S, ^2D)$	$3.0x10^{-10}$	[15, 20]
(R9)	$N_2(C^3\Pi_u) + O(^3P) \rightarrow NO + N(^4S, ^2D)$	$3.0x10^{-10}$	[15, 20]
(R10)	$N_2(a'^1\Sigma_u^-) + O(^3P) \rightarrow NO + N(^4S, ^2D)$	$3.0x10^{-10}$	[15, 20]
(R11)	$N(^2D) + O_2 \rightarrow NO + O(^3P, ^1D)$	$7.5x10^{-12} * \sqrt{T/300K}$	[12]
(R12)	$N(^4S) + NO \rightarrow N_2 + O(^3P)$	$7.5x10^{-12} * T^{0.5}$	[12]

Table 1. Main reactions leading to the production and losses of O atoms in the discharge and post-discharge. T is temperature (K).

IV. Properties of FIWs through Capillaries in Synthetic Air

A. Experimental results

1. Discharge current, applied voltage, energy deposition

The incident, reflected and transmitted voltage, obtained from the back current shunts are shown in Fig. 5.a. The corresponding HV and LV electrode voltages for three different pressures are in Fig. 5.b.. The transmitted currents collected by the LV electrode, as well as calculated current emitted by the HV electrode, are in Fig. 5.c.. Finally, the deposited energy is shown in Fig. 5.d. The energy deposition, W, is obtained from,

$$W = P(T) = \frac{1}{Z}\int_{t'=0}^{T} U_{inc}(t')^2 - U_{ref}(t')^2 - U_{trans}(t')^2 dt', \quad T > 50\ ns \tag{12}$$

where Z is the cable impedance (50 Ohm), $P(t)$ is the energy deposition up to time t, and $U_{inc,ref,trans}(t)$ is the incident, reflected, or transmitted voltage.

The voltage on the HV electrode corresponds to the sum of the incident and reflected pulses. The spatially averaged electric field, E(t), is then,

$$E(t) = (U_{HV}(t) - U_{LV}(t))/d \tag{13}$$

where $U_{HV}(t)$ and $U_{LV}(t)$ are the voltages on the HV and LV electrodes on either sides of the capillary (shown in Fig. 5.b), and d is the distance between the electrodes (80 mm in this experiment).

The current through the HV electrode is obtained by comparing the reflected pulse in the case when the HV electrode is covered by an insulating material, and the reflected pulse in the presence of the air plasma. The reflected current obtained with the plasma is subtracted from that obtained with the insulating material.

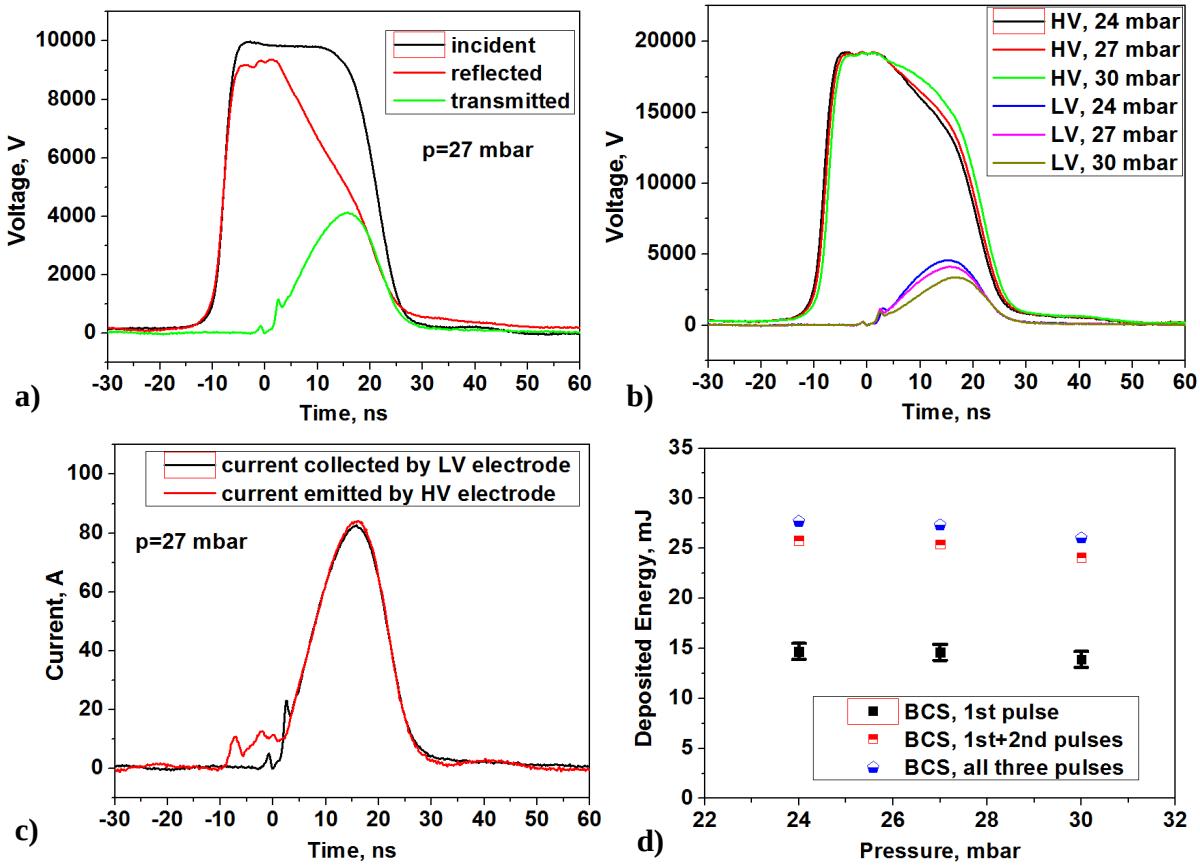

Figure 5. Properties of the FIWs. *a) Incident, reflected and transmitted pulses registered by the BCS; b) voltage on HV electrode (incident+reflected pulses), and on LV electrode (transmitted pulse), for different pressures; c) Current collected by LV electrode (transmitted current), and current through the HV electrode (see text); d) energy deposition.*

The difference between the two currents in Fig. 5.c can be explained by displacement current. Indeed, the current emitted by the HV electrode is calculated as a difference between the reflected current with no plasma and the reflected current with plasma in the discharge cell. This current consists of the conductivity current through the plasma and of the displacement current. While the FIW propagates along the tube, the conductivity current is low, and a significant portion of the displacement current returns to ground through the ground shield. This part of the signal corresponds to the low-current (10 A) step on the red curve. When the discharge gap is closed, the main current in the circuit is the conductivity current. At this stage, the current through HV and LV electrodes are almost equal.

The energy deposition is maximum during the first two pulses with there being little energy deposition during the third pulse. The energy deposition corresponds to about 1 eV/molecule after the first pulse.

2. Electric field

The reduced electric field E/N, for pressures of 24, 27 and 30 mbar and T_{gas} = 300 K, and transmitted current are shown in Fig. 6. Current in the middle of the tube as used in the 0D calculations is given by the green curves. To obtain these waveforms, the current flowing between -10 and 0 ns through the HV electrode, shown in Fig. 5.c, was changed to a flat "step" having a 5 ns duration. This was done to simulate the current at equal distance from the HV and LV electrodes. A comparison between the electric field calculated from BCS data and from capacitive probe data is also in Fig. 6. Note that the electric field based on BCS measurements is necessarily spatially averaged. The spike at -3 ns for the electric fields corresponds to the passing of the FIW near the detector. The discharge between 5 and 25 ns corresponds to the energy deposition phase with a high current and spatially uniform electric field.

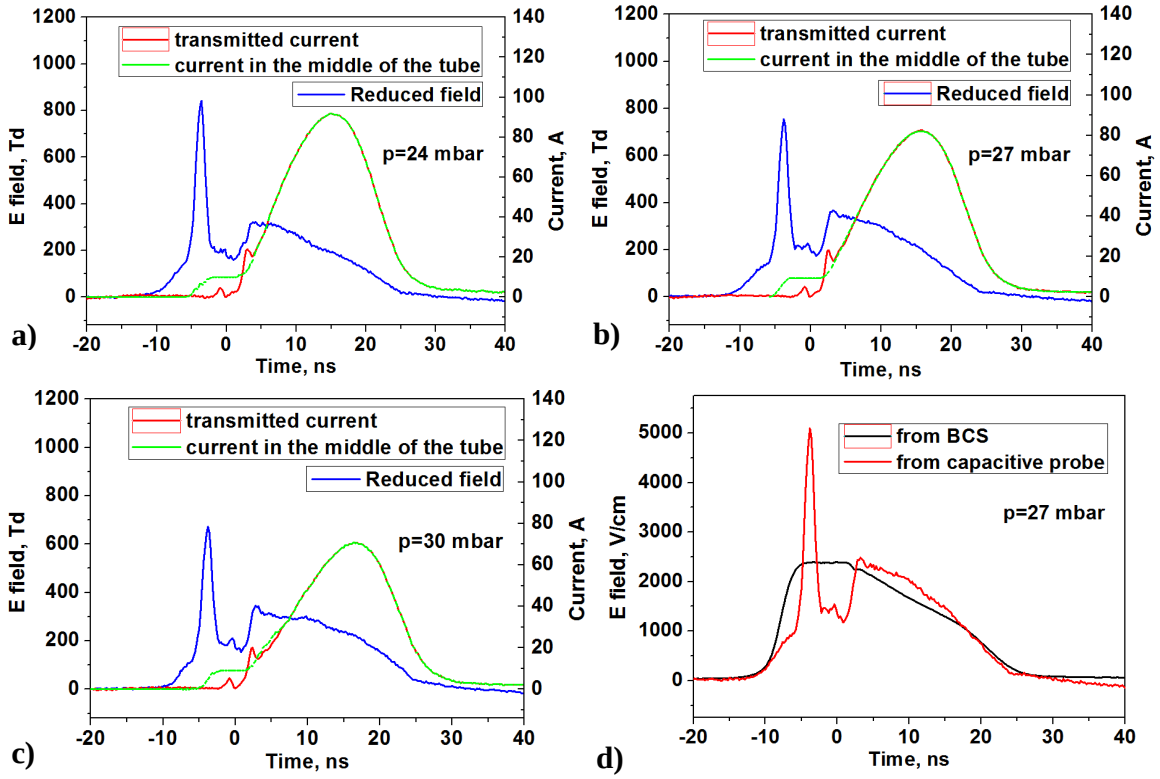

Figure 6. Experimental reduced electric field, transmitted current, and estimated current in the middle of the tube. a – 24 mbar, b - 27 mbar and c - 30 mbar. d) Comparison between BCS-based and capacitive probe-based electric field**.**

3. O atoms density

a) Actinometry

The expression for O atom density provided by actinometry, Eq. (11) has four primary contributions:

- A_1: The ratio of the line intensities, taking into account quenching, natural lifetime, intensity derivative with respect to time, detector sensitivity, ratio of direct electron impact excitation coefficients, and Argon density;
- A_2: Dissociative excitation contribution: $O_2 + e \rightarrow O + O(3p^3P) + e$;

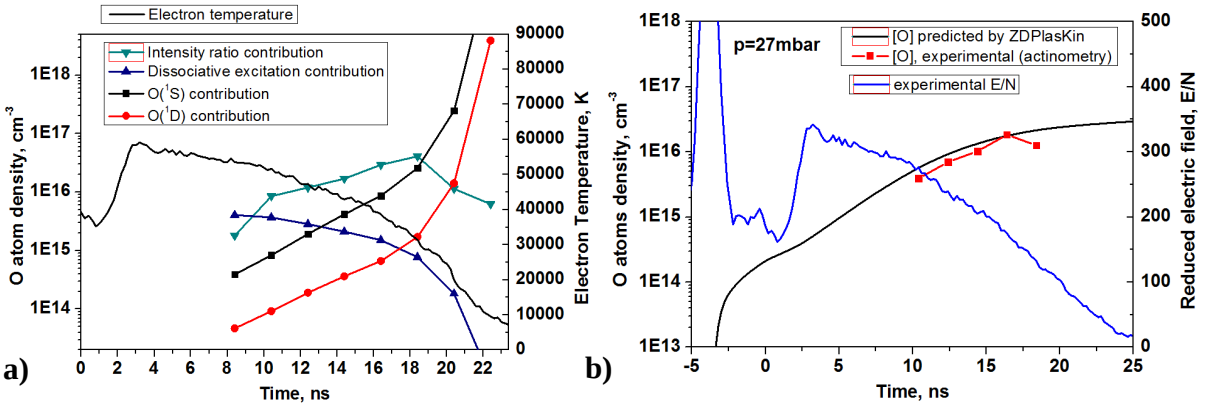

Figure 7. a) Experimental data (green) and contributions of all secondary processes that need to be subtracted from the experimental data (in blue, black and red). b) experimental O atom concentration, compared to the ZDPlasKin model prediction. *The reduced electric field is plotted for temporal reference.*

- A_3: Excitation of $O(3p^3P)$ from $O(^1S)$ metastable state by electron impact;
- A_4: Excitation of $O(3p^3P)$ from $O(^1D)$ metastable state by electron impact.

The peculiarity of the actinometry in the nanosecond discharge is that the density of the $O(^1S)$ and $O(^1D)$ metastable atoms can be high enough to influence population-depopulation balance of the measured $O(3p^3P)$ state[21]. If additional population of $O(3p^3P)$ from the metastables is important, the standard actinometry technique cannot be used. An additional analysis has been made to determine the limits of application of actinometry technique under the given experimental conditions.

Rate coefficients to estimate the input of the different processes (A_1-A_4) were calculated on the basis of the EEDF obtained from solution of Boltzmann equation in 2-term approximation in the given electric field using BOLSIG+ software. Then, kinetics of excited states was calculated, as discussed above, using ZDPlasKin code. The calculations were performed for the experimental profile of the electric field. Initial electron density was taken as a parameter of the calculations; it was demanded that the deposited energy during the pulse is equal for experiments and for the calculations. Contributions to the actinometry for A_1 - A_4 are shown in Fig. 7. As far as for five points within the interval 10-18 ns the conditions of the actinometry measurements are fulfilled, only these points were taken to calculate O-atoms density. The calculated O atom density is represented in Fig. 7.b together with experimental electric field and theoretical curve for O atom density calculated with the help of ZDPlasKin. In part IV.C, these results are compared with detailed 0D kinetic modeling.

b) TALIF

The dependence of the TALIF signal for O atom concentration *vs* laser energy was verified to be quadratic below the energy threshold of 150 µJ for O atoms and 10 µJ for Xe atoms. The wavelength-integrated signals of O and Xe atoms were compared to calculate the O atom concentration for a pressure of 27 mbar and a 2.2 µs delay after initial breakdown. The absolute values for other delays were then calculated taking into account the dependence of the calibration parameters on gas temperature.

The gas temperature in the post-discharge, measured through rotational spectroscopy of the second positive system of N_2, is shown in Fig. 8. The gas temperature increases during the first 2 µs to as high as 2000-2500 K. The O atom concentrations obtained by TALIF are shown in Fig. 9 for 27 mbar pressure and compared with actinometry results. Two cases are presented for quenching coefficients for O atoms being constant with gas temperature, or varying as $\sqrt{T/300K}$. The blue line corresponds to complete dissociation, where all O_2 molecules from the initial gas mixture are converted to O atoms. It was assumed that the quenching of the $O(3p^3P)$ state by O atoms is half that by O_2 molecules. This results in there being no effect of O_2 quencher depletion with increasing O atom density. The maximum error of the measurements is estimated to be 50%. The square root dependence fails at high temperatures, leading to measured values higher than the theoretical maximum of complete dissociation of O_2.

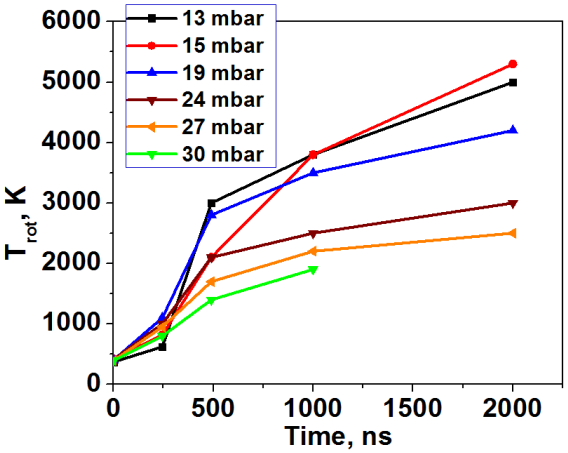

Figure 8. Gas temperature as a function of time after the initial discharge pulse.

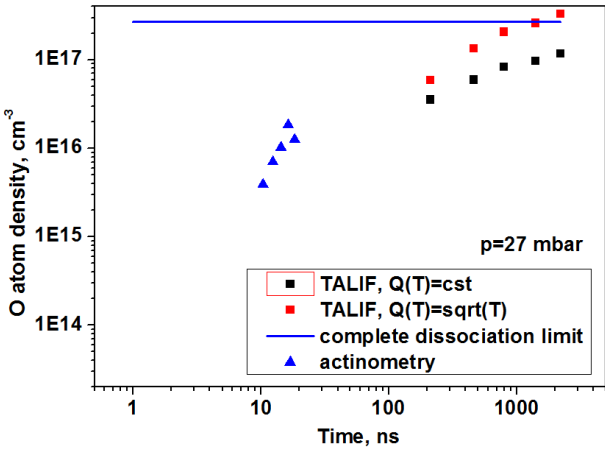

Figure 9. TALIF O atom data and actinometry results for 27 mbar pressure, and complete dissociation limit (total O atom density available from the gas initial composition and density).

B. Predictions of plasma properties from the 2D modeling

Results of the 2-d modeling of the FIW discharge in the capillary are shown in Fig. 10-13 for the experimental condition of 27 mbar. The electron impact ionization source S_e at the FIW front and the electric potential φ are shown in Fig. 10 at t = 3.0, 5.6 and 8.0 ns. The computational domain shown here includes the tube wall (top) and part of the HV (left) and LV (right) electrodes. Note that the radial scale has been expanded by a factor of 18 so that detail in the capillary tube can be observed which would otherwise be obscured by the large aspect ratio of the capillary. The FIW front crosses the 8 cm distance between the electrodes in about 9 ns, which produces a mean wave speed around 0.9 cm/ns or 9×10^8 cm/s. During its propagation, the structure of the ionization front does not significantly change and its peak remains on the axis. However, the

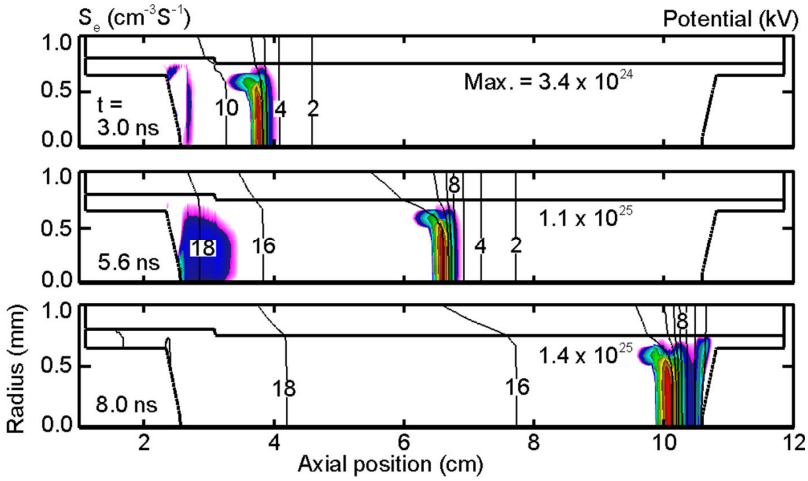

Figure 10. The electron impact ionization rate Se and the electric potential φ at t=3.0, 5.6 and 8.0 ns during the FIW discharge in the capillary. The high and low voltage electrodes are located at the left and right ends of the tube and the top is the dielectric tube wall. Contours are on a log scale over 4 decades.

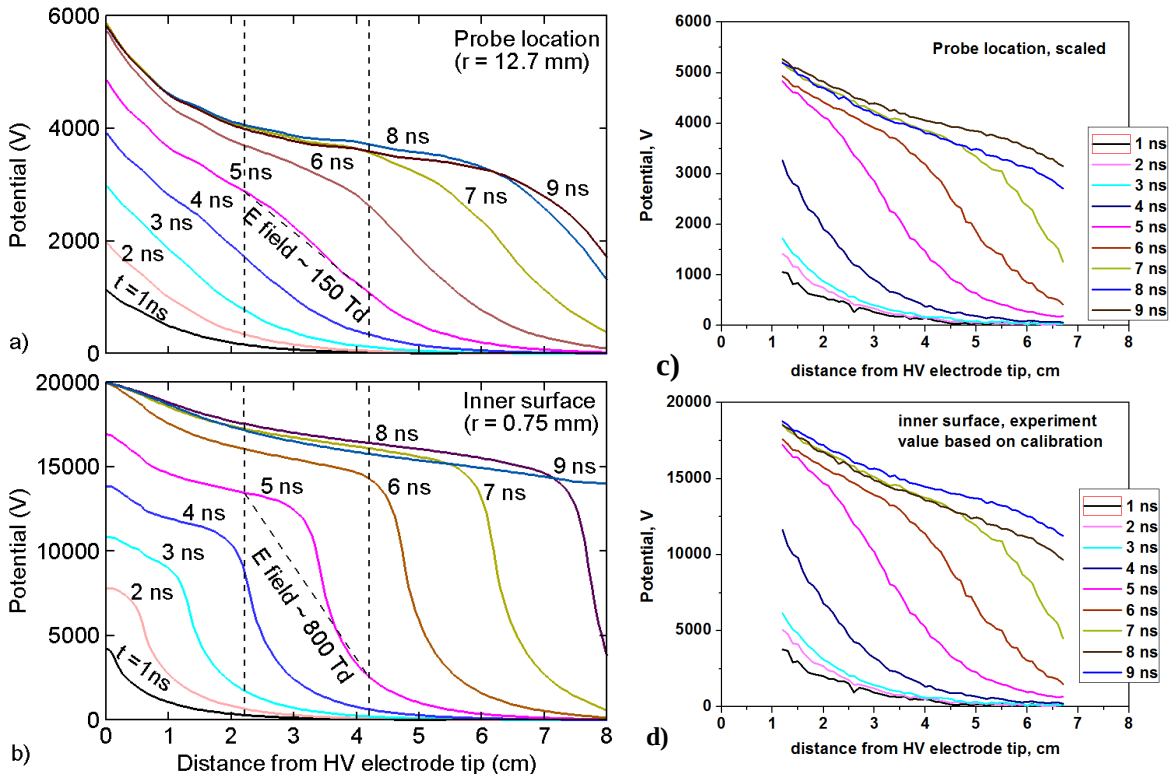

Figure 11.The axial potential profiles φ(z) during the FIW discharge at t = 1- 9 ns at the radial locations of (a) the tip of the capacitive probe in the experiments, r=12.7 mm, and (b) the inner surface of the capillary, r=0.75 mm. The two vertical dash lines mark the region between z = 22 and 42 mm from the HV tip where the electric field is measured in the experiments. Experimental curves are shown in c) scaled to match numerical values, and d) based on experimental calibration as described in Sec. II.

magnitude of the peak S_e increases from 3.4×10^{24} cm^{-3} s^{-1} near the HV electrode to 1.4×10^{25} cm^{-3} s^{-1} near the LV electrode. This increase results partly because the voltage on the HV electrode rises between t = 0-6 ns, which produces a small region of additional ionization near the HV electrode at t = 5.6 ns. The increase is also partly a result of the decreasing distance between the FIW front and the LV electrode, which produces a continuously increasing electric field in front of the FIW as the LV electrode is approached. This latter effect can be seen from the tight clustering of the potential contour lines in front of the FIW at t = 8.0 ns.

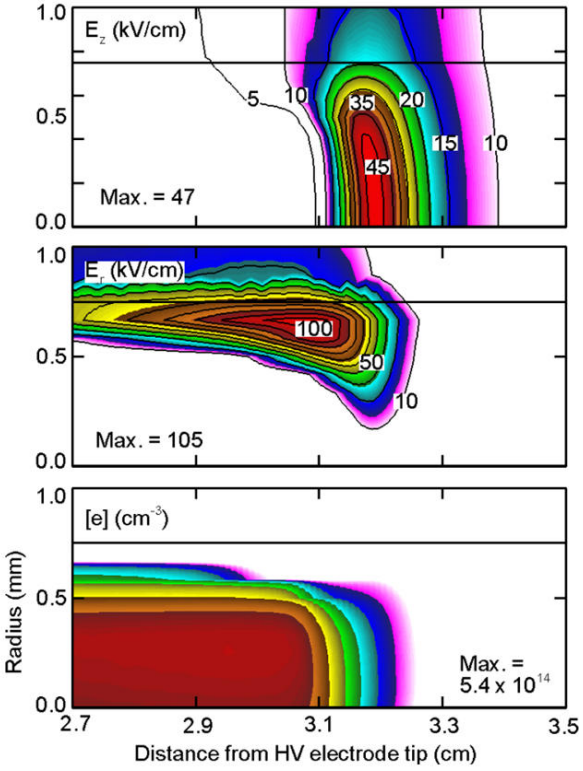

Figure 12.The instantaneous axial (a) and radial (b) electric fields E_z and E_r and the electron density n_e (c) at the FIW front at t = 5 ns. Contours are on a log scale over 4 decades for n_e.

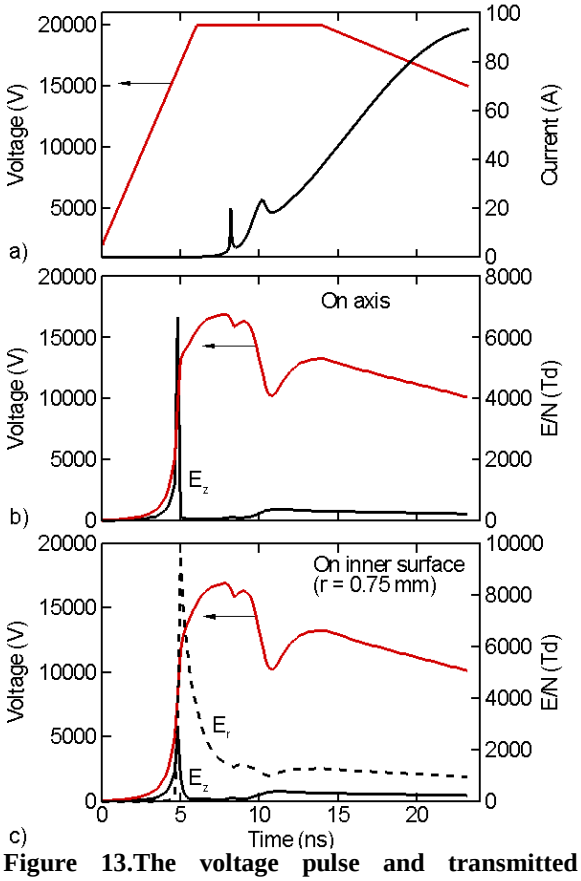

Figure 13.The voltage pulse and transmitted current of the FIW capillary discharge (a), and the time dependences of potential and electric fields on the tube axis (b) and the inner surface (c) at z = 32 mm from the HV electrode tip.

To make comparisons with the experiments, the electric potential $\varphi(z)$ as a function of the axial distance z (measured from the HV tip) is plotted in Fig. 11 at times t= 1- 9 ns. Values are shown at two radial locations, a) the tip of the capacitive probe, r = 1.27 cm, and b) the inner surface of the capillary, r = 0.075 cm. During the FIW propagation, the shapes of the $\varphi(z)$ profiles at the probe location are quite similar to the scaled experimental profiles shown in c). Note that the times in Fig. 11.c were shifted to match the numerical timestamps. The profiles are rather smooth and lack sharp gradients. If one estimates the peak reduced electrical field using $\varphi(z)$ at t = 5 ns and between z = 2.2 and 4.2 cm (the two vertical dash lines) as in the experiments, E/N is about 150 Td. Taking into account the scaling factor for potential (~ 4.8) between Fig. 11.c and Fig. 11.d, this corresponds to a peak E/N ≈ 720 Td, which is close to the measured peak E/N value in Fig. 6.b (around t = -3.6 ns). This agreement suggests that the FIW dynamics captured by the present 2-D modeling are consistent with those in the experiments.

While in the experiments, $\varphi(z)$ profiles along the inner capillary surface need to be inferred from the capacitive probe measurements, they can be obtained directly in the simulations as shown in Fig. 11.b. Compared to $\varphi(z)$ at the position of the probe, besides the different amplitudes, the primary difference between $\varphi(z)$ at the two radii is that the $\varphi(z)$ profiles on the inner surface show sharper gradient in potential moving from left to right. These sharp gradients correspond to the instantaneous axial locations of the FIW. If we again estimate the peak E/N in the same region between z = 2.2 and 4.2 cm directly using the $\varphi(z)$ in Fig. 11b (without the scaling factor), the average E/N is

about 800 Td, which is only slightly higher than the experimental value. We note the maximum E/N in this region at the leading edge of the FIW is about 2000 Td. However, given the fast speed of the FIW and the finite spatial and temporal resolution of the capacitive probe, the averaged E/N value is probably a more useful quantity to compare with the experiments.

The lack of sharp gradients for the potential curves at the location of the probe is not unexpected. From a physical point view, inside the capillary tube the FIW front separates an ionized, conductive region behind the FIW from the neutral, non-conductive region in front of the FIW. The potential inside the conductive channel is essentially the HV potential (minus the voltage drop due to the plasma resistivity). A large voltage drops occurs across the FIW. At the location of the probe, there is no such separation since the ambient air remains neutral and acts simply as a dielectric. From a computational viewpoint, there is a large contribution of space charge inside the capillary to the Poisson's equation which is capable of producing sharp potential gradients, while at the probe location, the lack of space charge reduces the Poisson's equation to a homogeneous Laplace equation, which tends to produce smooth solutions.

To better characterize the structure of the FIW, the axial and radial electric fields E_z and E_r, and the electron density n_e are shown in Fig. 12 at t = 5 ns. While E_z at the inner surface is about 20 kV/cm, its peak value on the axis is much higher, about 45 kV/cm. Slightly behind the FIW front, there is a narrow and elongated region near the wall where the radial electric field E_r reaches its peak, round 100 kV/ cm, much higher than that of E_z as a consequence of wall charging and sheath formation. The high E_r in this region may be understood from the spatial profile of n_e. The plasma channel that occupies the central region of the capillary has a high electron density $n_e = 5.4 \times 10^{14} cm^{-3}$, and high conductivity. As a result, the electric potential within the plasma column is close to the HV voltage. So there exists a large potential difference in the radial direction between outer edge of the plasma channel and the wall of the tube, culminating in the sheath, which results a large E_r.

The computed time dependence of the transmitted current, and the axial and radial electric fields at z = 3.2 cm on the tube axis and the inner surface of the wall are shown in Fig. 13. The computed current has a similar shape to that found in the experiments as shown in Fig. 6. The peak value of around 90 A also compares favorably with the measurements. As in Fig. 6, there are two small peaks in the computed current around t = 8.5 ns and 10.5 ns. The first peak represents the arrival of the FIW front at the LV electrode while the second peak is the return strike, in which the LV electrode launches a secondary ionization wave that travels backward towards the HV electrode with a high speed inside the already formed plasma channel. The closing of the gap by the forward FIW and the return strike are also reflected on the potential traces as the two dips in Fig. 13.b and 13.c around the same times. The potential curves at the axis and the inner surface of the tube are nearly identical, because the high electron density spreads the electric potential across the capillary radius. On the other hand, the electric fields at these two locations have different characteristics. On the axis, only E_z exists and its maximum value is about 7000 Td. The narrow width (in time) of E_z results from both the thinness of the FIW front as well as its high speed. On the inner surface, E_z is smaller and around 2500 Td with a similar shape as that on the axis. The radial electric field E_r is, however, much higher, about 10,000 Td, and has much wider extent, which corresponds to the larger axial extension of the high E_r region as shown in the Fig. 12.

C. 0D kinetic model results

The electrical current shown in Fig. 6 was used as input data to the 0d kinetics model, together with the parameters that were discussed in part III.B. The resulting reduced electric fields are shown in Fig. 14. There is good agreement for 24 and 27 mbar, while for 30 mbar the experimental data are somewhat higher than the results from the model. The shape of the electric field is in very good agreement with the electric field observed in the experiments. The first 1-2 nanoseconds correspond to the FIW front. At this stage, the field is spatially non-uniform and the 0D model reaches its lower bound in time for applicability. The low values of the electric field between 2 and 7 ns correspond to the discharge propagation phase, when the two electrodes are not yet connected by conduction current, and the fast ionization wave propagates towards the LV electrode. During this phase, a low (10 A) current is maintained through the tube section. The second peak, near 10 ns corresponds to the high current stage when the majority of the energy deposition occurs.

Results for energy deposition, calculated from experimental or numerical data, are shown in Table 2. In

Pressure	24 mbar	27 mbar	30 mbar
Model, IxE	14.6 mJ	14.6 mJ	13.6 mJ
Exp, BCS	14.7 mJ	14.6 mJ	13.9 mJ
Exp, IxE	14.8 mJ	15.2 mJ	15.1 mJ

Table 2. Deposited energy, computed from experimental and numerical values

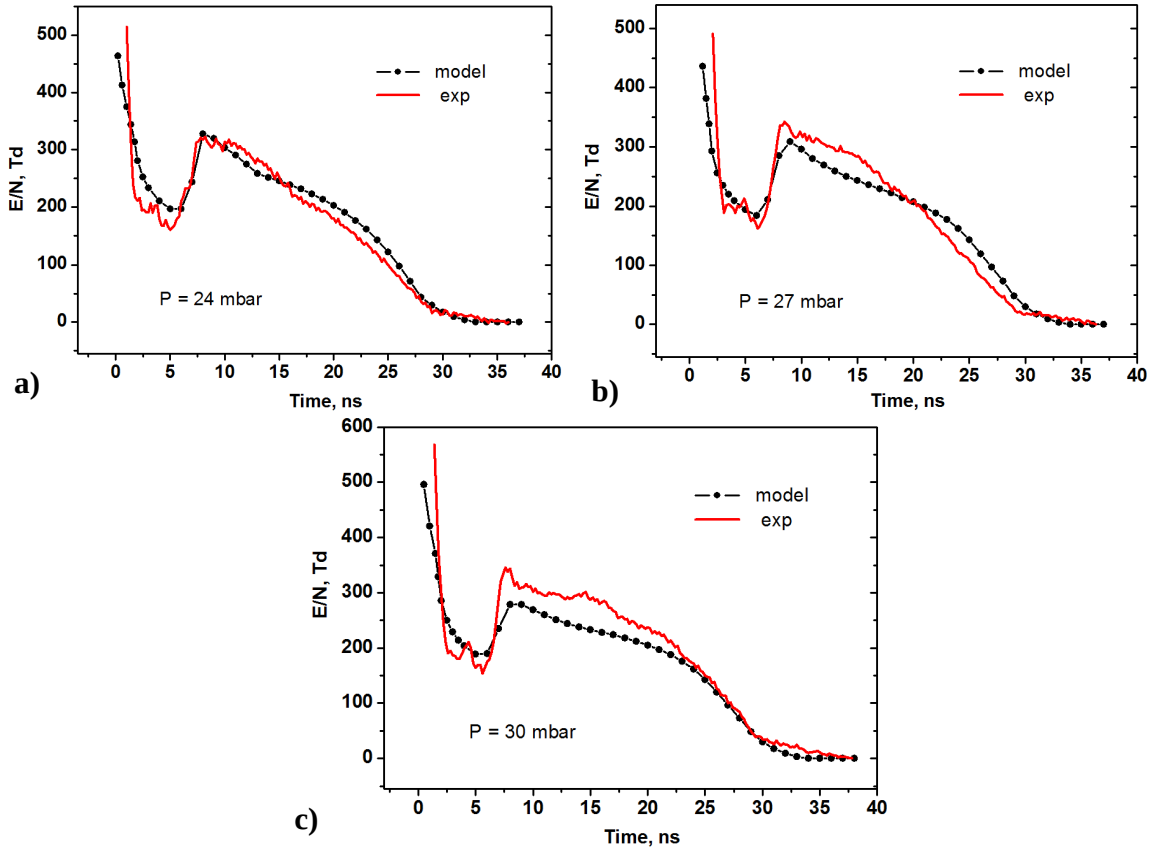

Figure 14. Reduced electric field calculated from the 0D kinetic model, compared to experiment. a) 24 mbar; b) 27 mbar; c) 30 mbar.

the experiments, two approaches were used. The first simply consisted in integrating the *IxE* product. Here, the experimental values of the current were taken from the back current shunt measurements, and the experimental values of the electric field were obtained by the calibrated capacitive probe, as described above. In the second method, the difference in integrals of incident and reflected current pulses measured in the cable were used taking into account the transmitted current. All of these signals were obtained from the BCS detectors, as described in Sec. II. The experimental BCS-based and numerical energy inputs agree very well. As such, the experimental E field for 30 mbar may have been overestimated.

The O atom density, calculated by the 0D model, is plotted in Fig. 15 and compared to both actinometry and TALIF values. There is good agreement between the calculations and the actinometry measurements during the discharge in the first pulse. This agreement validates the high dissociation degree obtained numerically after the first pulse.

A distinctive feature of the experiments presented in Fig.15 is that already after the first pulse the O-atoms density is extremely high. Reactions (R8,R9) were for the first time proposed in Ref. 15 to explain the dynamics of a fast gas heating of N_2:O_2 mixture at high degree of dissociation of molecular oxygen:

$$N_2(B^3\Pi_g) + O(^3P) \rightarrow NO + N(^4S, ^2D) \quad \text{(R8)}$$

$$N_2(C^3\Pi_u) + O(^3P) \rightarrow NO + N(^4S, ^2D) \quad \text{(R9)}$$

Rate constants of these reactions were proposed using the analysis of the experimental data on $N_2(A^3\Sigma_u^+, v = 7)$ quenching by atomic oxygen[22] and were taken to be $k \approx 7.5 \cdot 10^{-11}$ cm^3/s. In a later paper[20], higher values of the rate constants, $k_8 = k_9 = 3 \cdot 10^{-10}$ cm^3/s, were suggested on the basis of O(^{3}P), N(^{4}S) and NO densities, measured in the afterglow of a pulsed nanosecond discharge in air at P = 100 Torr. In the present calculations, data suggested in Ref. 20 were used (see Table 1).

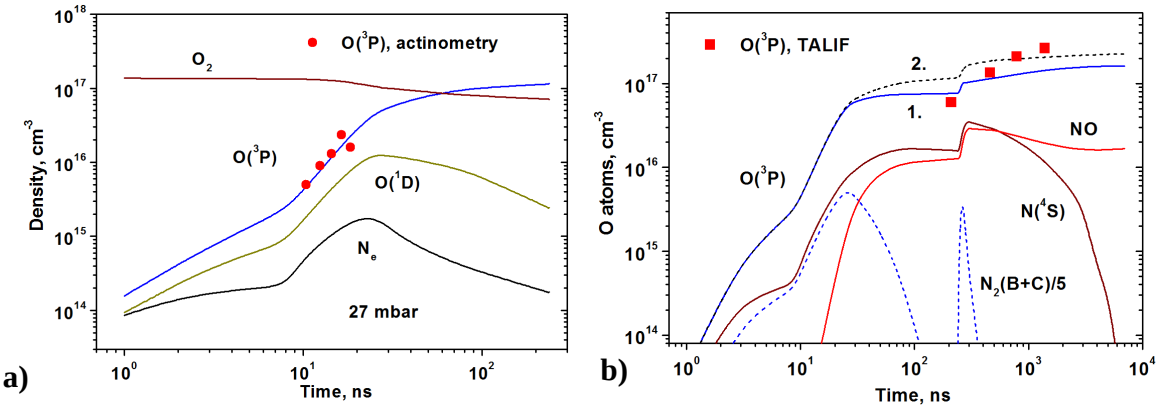

Figure 15. $O(^3P)$ atom density, and other main species, calculated by the 0D model, compared to experimental data. a) first pulse and early post-discharge, with actinometry measurements; b) 2 µs time scale, with TALIF measurements. *Note: for TALIF values, the $\sqrt{T/300K}$ approximation was used for quenching coefficient behavior with temperature.*

To underline the importance of quenching of excited nitrogen molecules by atomic oxygen, Fig.15 b gives the results of calculations of O-atoms density for two cases: taking into account reactions (R8, R9, R10), curve 1; and without taking into account the aforementioned reactions, curve 2. Densities of N(^{4}S), NO, and summary density of electronically excited states of molecular nitrogen, $N_2(B^3\Pi_g) + N_2(C^3\Pi_u)$ are also given. With increase of O-atoms density, quenching of excited nitrogen molecules, $N_2(A^3\Sigma_u^+)$, $N_2(B^3\Pi_g)$, $N_2(C^3\Pi_u)$ and $N_2(a'^1\Sigma_u^-)$ takes place by O-atoms, producing N(^{4}S, ^{2}D) atoms and NO molecules. So, the O_2 dissociation *via* collisions with excited nitrogen molecules becomes less efficient and O atom density decreases in comparison with O atom density calculated without reactions (R8, R9, R10). As seen from Fig. 15, taking into account reactions (R8, R9, R10), allows to obtain an agreement between the calculation results and the measurements at t = 210 and 460 ns. However, the temporal behavior of the O-atom density *vs* time is more sharp in the experiments than in the calculations. The high value for TALIF measurements at 1-2 µs can be caused by an overestimate of quenching coefficients (as the temperature, and hence the uncertainty in quenching values, rises with time).

V. Conclusions

Development of a fast ionization wave in a capillary tube in air at moderate pressure (20-30 mbar) was experimentally and numerically investigated. FIW influence on the gas mixture has been analyzed on the basis of measurements and numerical calculations of plasma parameters and density of atomic oxygen in the discharge and in the afterglow.

Electrical current, electric field and spatial distribution of the electric potential were compared to predictions from a 2D axisymmetric model describing plasma initiation and breakdown on a 20 ns time scale. Both experimental measurements and numerical calculations produce similar values of the FIW front velocity, about 1 cm/ns, and similar shapes and values of the electrical current, about 80-90 A at the peak. The 2D numerical modeling describes the detailed fast ionization wave front structure, as well as the smoothing of the potential observed in the local electric potential measurement produced by the capacitive probe. In addition, the results from this simulation provide some insight in the early phase, spatially inhomogeneous plasma parameters.

Measured values of electrical current were taken as a basis for the 0D kinetic modeling, taking into account the kinetics of excited species in the discharge and afterglow, and a fast energy release due to relaxation of electronically excited atoms and molecules, so called fast gas heating. There was good agreement between the calculated and measured values of longitudinal electric field behind the breakdown front and with O atom density. The main distinctive feature of FIWs in capillary tubes is the high energy density at relatively high electric fields. This results in an efficient excitation of electronic levels and dissociation *via* electronically excited levels. High atomic oxygen density is a good indication of the efficiency of these processes. Ar actinometry and TALIF produced O atom densities that are in reasonable agreement with the 0D model based on absolute values.

Acknowledgments

The authors are thankful to J. Guillon for technical assistance. The work was partially supported by French National Agency, ANR (PLASMAFLAME Project, 2011 BS09 025 01), AOARD AFOSR, FA2386-13-1-4064 grant (Program Officer Prof. Chiping Li), and by PICS-RFBR grant (5745-11.02.91063-a/5745). The work at the University of Michigan was supported by the United States Department of Energy Office of Fusion Energy Science and the National Science Foundation.

References

[1]Starikovskaia, S. M., and Starikovskii, A. Yu., "Plasma-Assisted Ignition and Combustion" in: *Handbook of Combustion, Vol. 5: New Technologies*, Lackner M, Winter F, Agarwal A K, eds. WILEY VCH Verlag GmbH & Co. KGaA, 2010, p. 71.

[2]Adamovich, I. V., Choi, I., Jiang, N., Kim, J-H., Keshav, S., Lempert, W. R., Mintusov, E., Nishihara, M., Samimy, M., and Uddi, M., "Plasma assisted ignition and high-speed flow control: non-thermal and thermal effects", *Plasma Sources Science and Technology*, Vol. 18, No. 3, 2009, 034018 (13 pp).

[3]Kosarev, I. N., Aleksandrov, N. L., Kindysheva, S. V., Starikovskaia, S. M., and Starikovskii, A. Yu., "Kinetics of ignition of saturated hydrocarbons by nonequilibrium plasma: CH4-containing mixtures" *Combustion and Flame*, Vol. 154, No. 3, 2008, pp. 569-586.

[4]Popov, N. A., "Fast gas heating in a nitrogen-oxygen discharge plasma: I. Kinetic mechanism", *Journal of Physics D: Applied Physics*, Vol. 44, No. 28, 2011, 285201 (16 pp).

[5]Nishihara, M., Takashima, K., Rich, J. W., and Adamovich, I. V., "Mach 5 bow shock control by a nanosecond pulse surface dielectric barrier discharge", *Physics of Fluids*, Vol. 23, No. 6, 2011, 066101 (11 pp).

[6]Anikin, N., "Experimental Investigation of Electrodynamic Characteristics of the Fast Ionization Wave in Molecular Gases", Ph.D. Dissertation, Moscow Institute of Physics and Technology, Moscow, Russia, 2000 pp. 32-35 (in Russian).

[7]Katsch, H.-M., Tewes, A., Quandt, E., Goehlich, A., Kawetzki, T., and Dobele, H. F., "Detection of atomic oxygen: Improvement of actinometry and comparison with laser spectroscopy", *Journal of Applied Physics*, Vol. 88, No. 11, 2000, pp. 6232-6238.

[8]Henriques, J., Villeger, S., Levaton, J., Nagai, J., Santana, S., Amorim, J., and Ricard, A., "Densities of N- and O-atoms in N2–O2 flowing glow discharges by actinometry", *Surface and Coatings Technology*, Vol. 200, No. 1-4, pp. 814-817.

[9]Fuller, N. C. M., Malyshev, M. V., Donnelly, V. M., and Herman, Irving P., "Characterization of transformer coupled oxygen plasmas by trace rare gases-optical emission spectroscopy and Langmuir probe analysis", *Plasma Sources Science and Technology*, Vol. 9, No. 2, pp. 116-127.

[10]Piper, L. G., Clyne, M. A. A., and Monkhouse, P. B., "Electronic energy transfer between metastable argon atoms and ground-state oxygen atoms", *Journal of the Chemical Society, Faraday Transactions 2*, Vol. 78, 1982, pp. 1373-1382.

[11]Computer code ZDPlasKin, ver. 1.3B10 (Sept 2012), Pancheshnyi, S., Eismann, B., Hagelaar, G.J.M., Pitchford, L.C., University of Toulouse, LAPLACE, CNRS-UPS-INP, Toulouse, France, 2008.

[12]Kossyi, I. A., Kostinsky, A. Y., Matveev, A. A., and Silakov, V. P., "Kinetic scheme of the non-equilibrium discharge in nitrogen-oxygen mixtures", *Plasma Sources Science and Technology*, Vol. 1, No. 3, 1992, pp. 207-220.

[13]Salmon, A., "Actinometry of atomic oxygen in a capillary nanosecond discharge", Master thesis, LPP, Ecole Polytechnique, Palaiseau, France, 2013, pp 11-33.

[14]Niemi, K., Schulz-von der Gathen, V., and Döbele, H. F., "Absolute atomic oxygen density measurements by two-photon absorption laser-induced fluorescence spectroscopy in an RF-excited atmospheric pressure plasma jet", *Plasma Source Science and Technology*, Vol. 14, No. 2, 2005, pp. 375-386.

[15]Klochko, A. V., Lemainque, J., Popov, N. A., Booth, J.-P., and Starikovskaia, S. M., "Study of fast gas heating in a capillary nanosecond discharge in air. TALIF O atoms measurements and kinetic modeling", *Proc. of 51st AIAA Aerospace Sciences Meeting, 7-10 January 2013*, Grapevine, Texas, AIAA 2013-0574 (18 pp).

[16]Xiong, Z., and Kushner, M. J., "Atmospheric pressure ionization waves propagating through a flexible high aspect ratio capillary channel and impinging upon a target", *Plasma Sources Science and Technology*, Vol. 21, No. 3, 2012, 034001 (13 pp).

[17]Xiong, Z., Robert, E., Sarron, V., Pouvesle, J-M., and Kushner, M. J., "Dynamics of ionization wave splitting and merging of atmospheric-pressure plasmas in branched dielectric tubes and channels", *Journal of Physics D: Applied Physics*, Vol. 45, No. 27, 2012, 275201 (19 pp).

[18]Braginsky, O. V., Vasilieva, A. N., Klopovskiy, K. S., Kovalev, A. S., Lopaev, D. V., Proshina, O. V., Rakhimova, T. V.,and Rakhimov, A. T., "Singlet oxygen generation in O2 flow excited by RF discharge", *Journal of Physics D: Applied Physics*, Vol. 38, No. 19, 2005. pp 3609-3625.

[19]Kovalev, A. S., Lopaev, D. V., Mankelevich, Yu. A., Popov, N. A., Rakhimova, T. V., Poroykov, A. Yu., and Carroll, D. L. "Kinetics of $O_2(b^1\Sigma_g)$ in oxygen RF discharges", *Journal of Physics D: Applied Physics*, Vol. 38, No. 14, 2005, pp 2360-2370.

[20]Burnette, D., Shkurenkov, I., Adamovich, I. V., and Lempert, W. R., "An examination of nitric oxide kinetics in a plasma afterglow with significant vibrational loading", *52nd AIAA Aerospace Sciences Meeting*, National Harbor, MD, January 2014.

[21]Gordillo-Vazquez, F. J., and Kunc, J. A., "Diagnostics of plasmas with substantial concentrations of atomic oxygen", *Physical Review E*, Vol. 51, No. 6, 1995, pp. 6010-6015.

[22]De Benedictis, S., and Dilecce, G., "Rate constants for deactivation of $N_2(A)$ v = 2-7 by O, O_2, and NO", *Journal of Chemical Physics*, Vol. 107, No. 16, 1997, pp. 6219-6229.